AUTHOR(S):

Kikukawa, Motoyuki; Asamura, Kazushi; Zushi, Takahiro; Kurita, Satoshi; Kojima, Hirotsugu

TECHNICAL REPORT

Open Access

Check for updates

Development of miniaturized pick-up amplification circuit for plasma particle detectors on board satellites
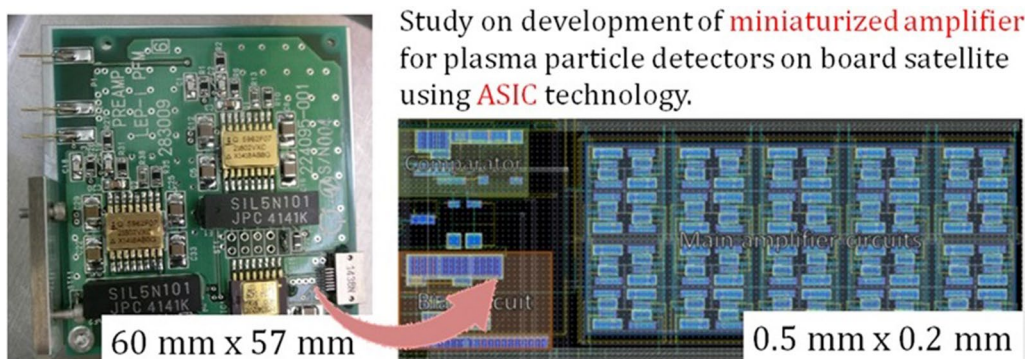
Motoyuki Kikukawa[1]* , Kazushi Asamura[2], Takahiro Zushi[3], Satoshi Kurita[1] and Hirotsugu Kojima[1]

Abstract

Plasma particles and waves are important observation targets in space plasmas for understanding the mechanisms of energy and momentum transfer between waves and particles because space plasmas are essentially collisionless. Multi-point observations are crucial for understanding the spatial–temporal variations of space plasmas. To realize such observations by a large number of satellites, onboard instruments should be miniaturized to reduce their required resources. This paper proposes a small amplifier for plasma particle detectors onboard satellites. This charge-sensitive amplifier converts an electron cloud emitted from the detector, for example a microchannel plate, to a current pulse that can be handled by a time-of-flight measurement circuit to determine the particle velocity and thus mass. The amplifier is realized using application-specific integrated circuit technology to minimize size. Its dimensions are estimated to be $2120\ \mu\text{m} \times 1680\ \mu\text{m}$, which are much smaller than those of a conventional amplifier. The response time of the proposed amplifier has a variation of less than 1.2 ns over the range of expected input levels. The amplifier can handle up to 2×10^7 signals per second and has a sensitivity of 1.5 V/pC at 20 °C.

Keywords: ASIC, Multi-point observation, Amplifier for time-of-flight technique

Graphical Abstract

60 mm x 57 mm

Study on development of **miniaturized amplifier** for plasma particle detectors on board satellite using **ASIC** technology.

0.5 mm x 0.2 mm

---

*Correspondence: kikukawa.motoyuki.75u@st.kyoto-u.ac.jp

[1] Research Institute for Sustainable Humanosphere, Kyoto University, Gokasho, Uji 611-0011, Japan
Full list of author information is available at the end of the article

Main text
Introduction
In situ observations of plasma particles and waves by satellites are essential for understanding the mechanisms

Springer Open

of energy transfer between particles and waves in space plasmas. For space plasmas, it is difficult to distinguish spatial variations from temporal ones based on single-satellite observations.

To overcome this problem, recent satellite fleet missions such as Cluster-II (Escoubet et al. 2001), THEMIS (Angelopoulos et al. 2008), and MMS (Burch et al. 2016; Tooley et al. 2016) have formation flights that consist of 4–5 satellites. However, a lot of resources are required for these multi-point missions, and opportunities for conducting these missions are limited. The use of small satellites is a feasible way to increase such opportunities. Attempts to miniaturize the instruments for detecting plasma waves have been made, including the development of dedicated devices based on an application-specific integrated circuit (ASIC) (Ozaki et al. 2016; Zushi et al. 2019). The circuits necessary for plasma wave detection can be integrated on a chip using ASIC technology. The size of such a dedicated device is 5 mm × 5 mm (Ozaki et al. 2016), which is small enough for the installation of plasma wave instruments on small satellites.

Particle measurements with mass discrimination are important because several ion species are often present in space plasmas. For example, plasma in the terrestrial magnetosphere consists of H^+, He^+, He^{++}, N^{++}/O^{++} group, N^+/O^+ group, and molecular ions. Previous studies have shown that the ion composition drastically changes with geomagnetic and solar activity (e.g., Young et al. 1982; Maggiolo and Kistler 2014). The ion composition affects the dispersion relation of electromagnetic ion cyclotron waves (e.g., Rauch and Roux 1982), which controls the propagation and resonance conditions for waves with particles (Summers and Thorne 2003). Mass-dependent variations of ion fluxes have also been reported (Gloeckler et al. 1985; Keika et al. 2022; Shelley et al. 1972; Williams 1981). Recently, energy transfer from one ion species to other species through wave–particle interactions has been detected using the Wave–Particle Interaction Analyzer (Katoh et al. 2013; Kitamura et al. 2018; Shoji et al. 2021; Asamura et al. 2021). Thus, mass-discriminated particle measurements are essential for understanding the dynamic variations of space plasmas. To adapt particle sensors to small satellites, the sensors need to be miniaturized in the same way that plasma wave instruments have been. Our group has developed a miniaturized amplifier for particle measurements (HERMES64) that provides particle counts accumulated during a given period (Saito et al. 2017). However, HERMES64 does not provide signals for time-of-flight (TOF) analysis which is used for the discrimination of ion species.

The TOF technique is based on the measurement of the time required for an incoming particle to move from a specific location to another inside a sensor. Since the TOF path length is known, the TOF technique provides information regarding particle velocity. The ASIC developed in the present study amplifies signals from a microchannel plate (MCP). The amplified signals can be used for TOF calculations to discriminate typical ion species in planetary magnetospheres and the solar wind. We present the design and specifications of the developed ASIC amplifier and demonstrate the performance of its prototype using laboratory experiments.
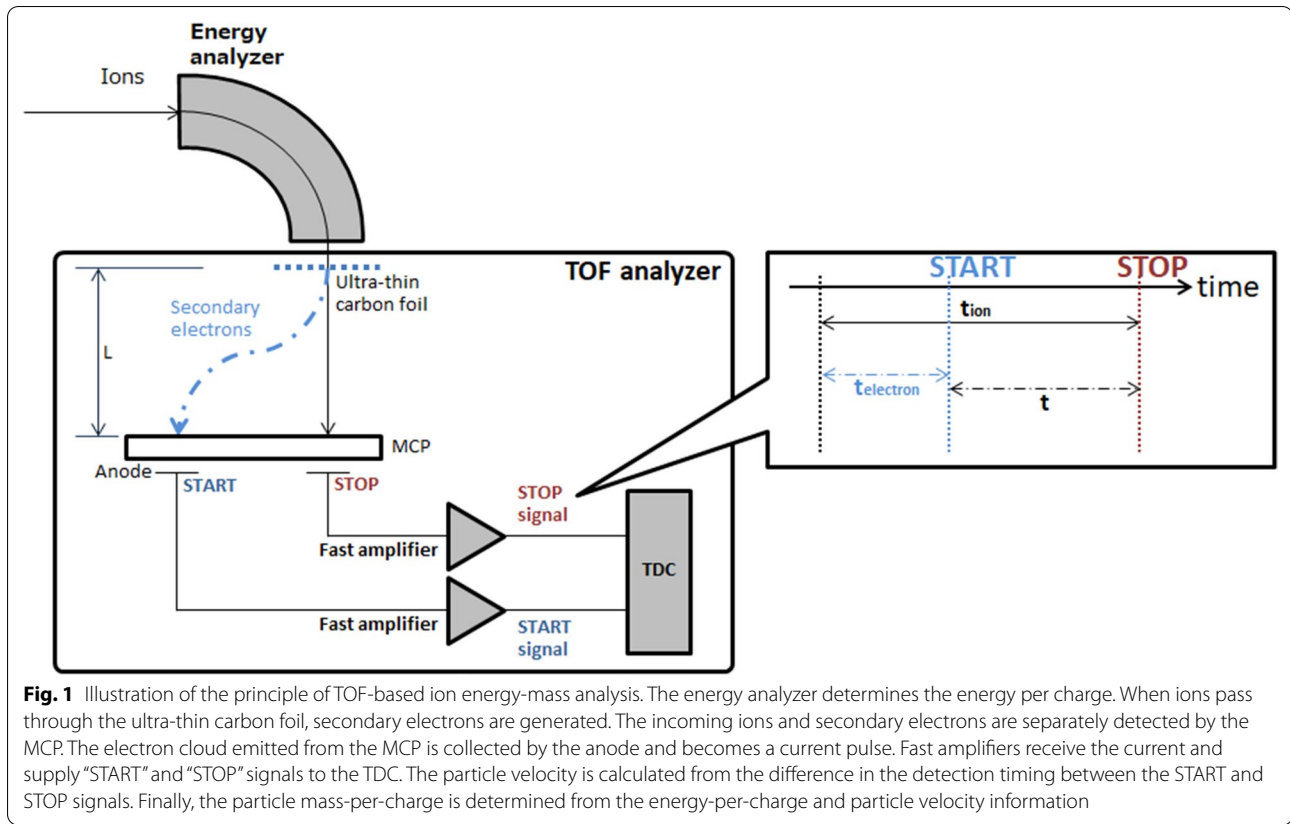
Instruments for plasma particle observations

Figure 1 schematically shows the principle of the TOF-based ion energy-mass analysis. The TOF technique is commonly used with an electrostatic energy-per-charge analyzer (ESA), which can be used to deduce particle mass-per-charge from the energy-per-charge and velocity information (Wüest 1998; Carlson and McFadden 1998, and references therein). A typical TOF system measures the difference of the detection times between two inputs onto an MCP; one input is the secondary electrons emitted from an ultra-thin carbon foil when an incoming particle passes through it (START signal) and the other input is the incoming particle itself (STOP signal). The mass of an ion is expressed as follows:

$$m = \left(\frac{2E}{L^2}\right) t_{ion}^2,$$

where m, E, L, and t_{ion} are the particle mass, energy, flight path length for ions, and flight time for ions, respectively. Therefore, the mass of ions can be obtained from t_{ion} if E and L are given.

Figure 2 shows photographs and a circuit block diagram of the conventional amplifier implemented in the low-energy particle experiment–ion mass analyzer (LEPi) (Asamura et al. 2018), which is a TOF-type ion energy-mass analyzer onboard the Arase satellite (Miyoshi et al. 2018). When a particle hits the MCP, it generates an electron cloud that produces a current pulse of 30-200 mV (at an input impedance of 50 Ω) with a duration of 1-2 ns. The amplifier provides timing signals with a pulse height of 3.3 V for the subsequent time-to-digital converter (TDC), which performs the TOF calculation. The LEPi has 15 azimuthal angular channels. Conventional amplifiers are installed on 15 identical boards arranged radially and connected in parallel, as shown in Fig. 2b. Two amplifiers are installed on each board, giving a total of 30 amplifiers in the LEPi. The size of each board is 6.0 cm × 5.7 cm. In the assembled configuration, the amplifier (which consists of 15 boards) consumes a volume of 230 cm² (total area of the bottom) × 7 cm (height).

Fig. 1 Illustration of the principle of TOF-based ion energy-mass analysis. The energy analyzer determines the energy per charge. When ions pass through the ultra-thin carbon foil, secondary electrons are generated. The incoming ions and secondary electrons are separately detected by the MCP. The electron cloud emitted from the MCP is collected by the anode and becomes a current pulse. Fast amplifiers receive the current and supply "START" and "STOP" signals to the TDC. The particle velocity is calculated from the difference in the detection timing between the START and STOP signals. Finally, the particle mass-per-charge is determined from the energy-per-charge and particle velocity information
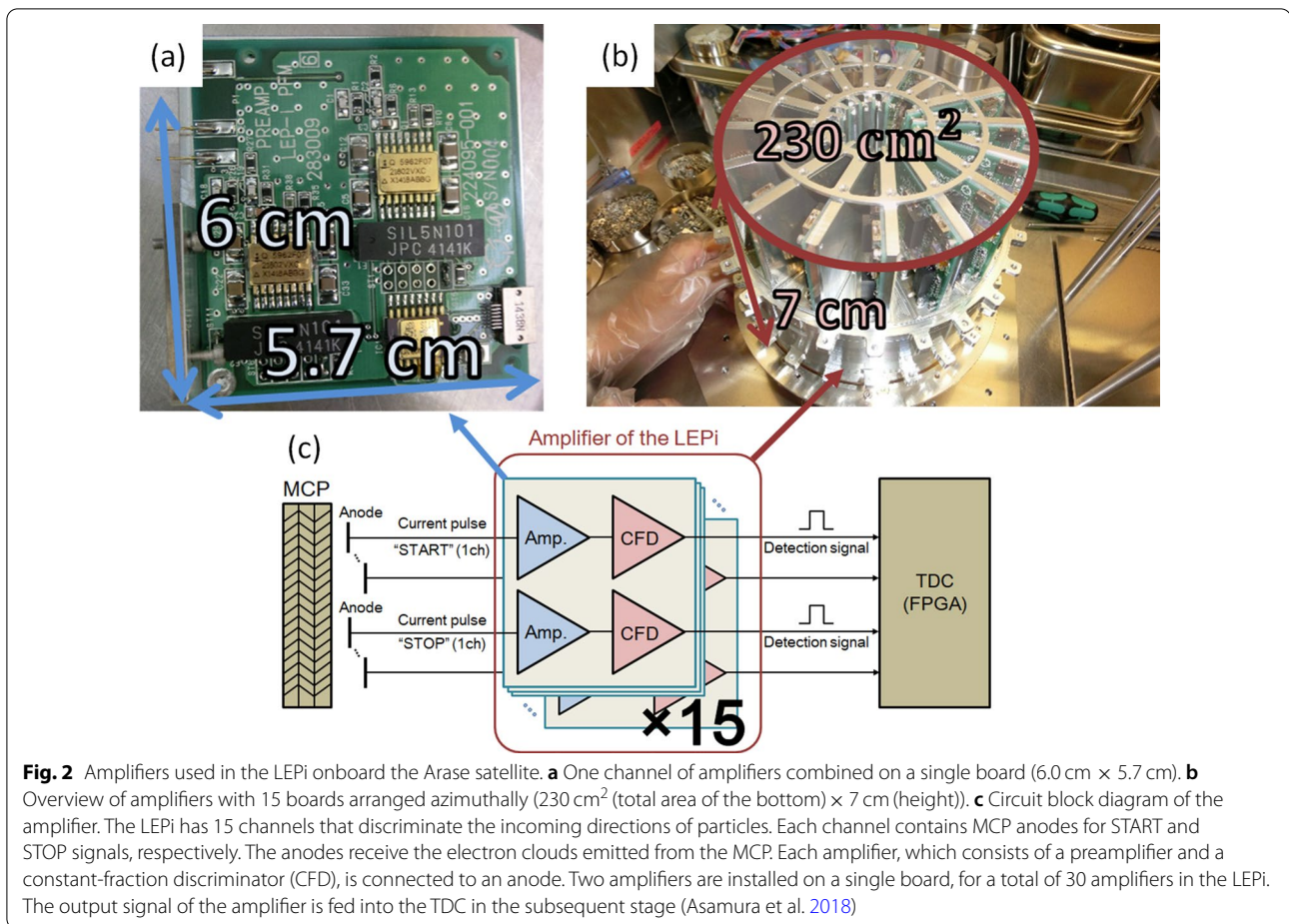
The proposed ASIC-based amplifier was developed for an ion energy-mass spectrometer for exploring plasma dynamics in the terrestrial magnetosphere. Since the major ion species in the terrestrial magnetosphere are $H^+, He^+, He^{++}, N^{++}/O^{++}$ group, N^+/O^+ group, and molecular ions, the required mass resolution ($\Delta m/m$) is below 0.5. Note that conventional ion energy-mass spectrometers measure mass per charge. Here, we consider a conventional ion energy-mass spectrometer that consists of an electrostatic energy-per-charge analyzer and a simple TOF velocity analyzer. Incident particles fly free inside the TOF measurement chamber. For this case, the mass resolution can be expressed as:

$$\frac{\Delta m}{m} = \frac{\Delta E}{E} + \frac{2\Delta t}{t},$$

where $m, E,$ and t are the particle mass, energy, and flight time inside the TOF measurement chamber, respectively (Wurz 2000). The energy resolution ($\Delta E/E$) is determined by the electrostatic energy-per-charge analyzer. We take 0.2 for $\Delta E/E$ since $\Delta E/E$ for the LEPi onboard the Arase satellite, which is a terrestrial inner magnetospheric mission (Miyoshi et al. 2018), is 0.13 to 0.16 (full width at half maximum) (Asamura et al. 2018). Thus, $\Delta t/t$ should be below 0.15. However, a higher ion

energy leads to a shorter flight time. If we take protons (the lightest ions) with an energy of 25 keV (the highest energy detectable by the LEPi), the flight time becomes 11 ns for the LEPi. Δt should be below 1.6 ns in this case. Thus, we took 1 ns as the required timing resolution for the proposed ASIC-based amplifier.

In previous satellite missions for investigating fast plasma phenomena in the terrestrial magnetosphere, the time resolutions of the ion instruments were 78 ms (ESA onboard the FAST satellite (Carlson et al. 2001)), 40 ms (ISA onboard the Reimei (INDEX) satellite (Asamura et al. 2003)), and 150 ms (FPI-DIS onboard the MMS satellite (Pollock et al. 2016)). Their sampling times for each energy step were 1.6, 1.3, and 2.3 ms, respectively. For defining the requirements for the proposed ASIC-based amplifier, we take a sampling time of 1 ms and a maximum count rate of 1000 counts/sample as an example observation. If we set 100 ns for the dead time due to the ASIC processing time, the saturation effects caused by the dead time will reduce the detected counts by 10 % at most. Assuming that the number of collision events of particles with a detector within the dead time of the ASIC obeys the Poisson distribution, we set the maximum processable count rate to 1×10^7/s for the proposed ASIC-based amplifier.

Kikukawa *et al. Earth, Planets and Space*   *(2022) 74:188*

Page 4 of 11

Fig. 2 Amplifiers used in the LEPi onboard the Arase satellite. **a** One channel of amplifiers combined on a single board (6.0 cm × 5.7 cm). **b** Overview of amplifiers with 15 boards arranged azimuthally (230 cm^2 (total area of the bottom) × 7 cm (height)). **c** Circuit block diagram of the amplifier. The LEPi has 15 channels that discriminate the incoming directions of particles. Each channel contains MCP anodes for START and STOP signals, respectively. The anodes receive the electron clouds emitted from the MCP. Each amplifier, which consists of a preamplifier and a constant-fraction discriminator (CFD), is connected to an anode. Two amplifiers are installed on a single board, for a total of 30 amplifiers in the LEPi. The output signal of the amplifier is fed into the TDC in the subsequent stage (Asamura et al. 2018)

Design of high-speed current detection circuit

We aim to greatly reduce the required resources of the circuits for particle measurements onboard satellites by developing an amplifier (hereafter referred to as the high-speed current detection circuit) for TOF measurements based on ASIC technology, which allows us to integrate the circuits into a single chip.
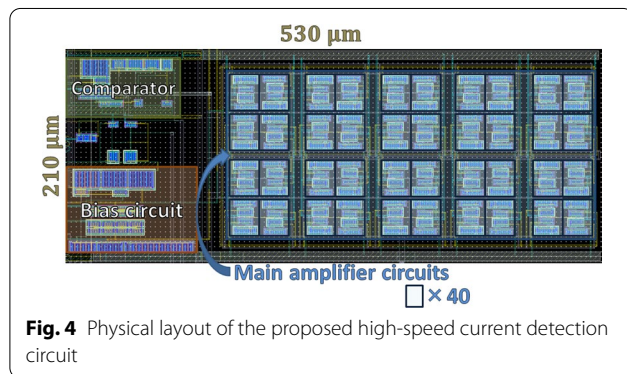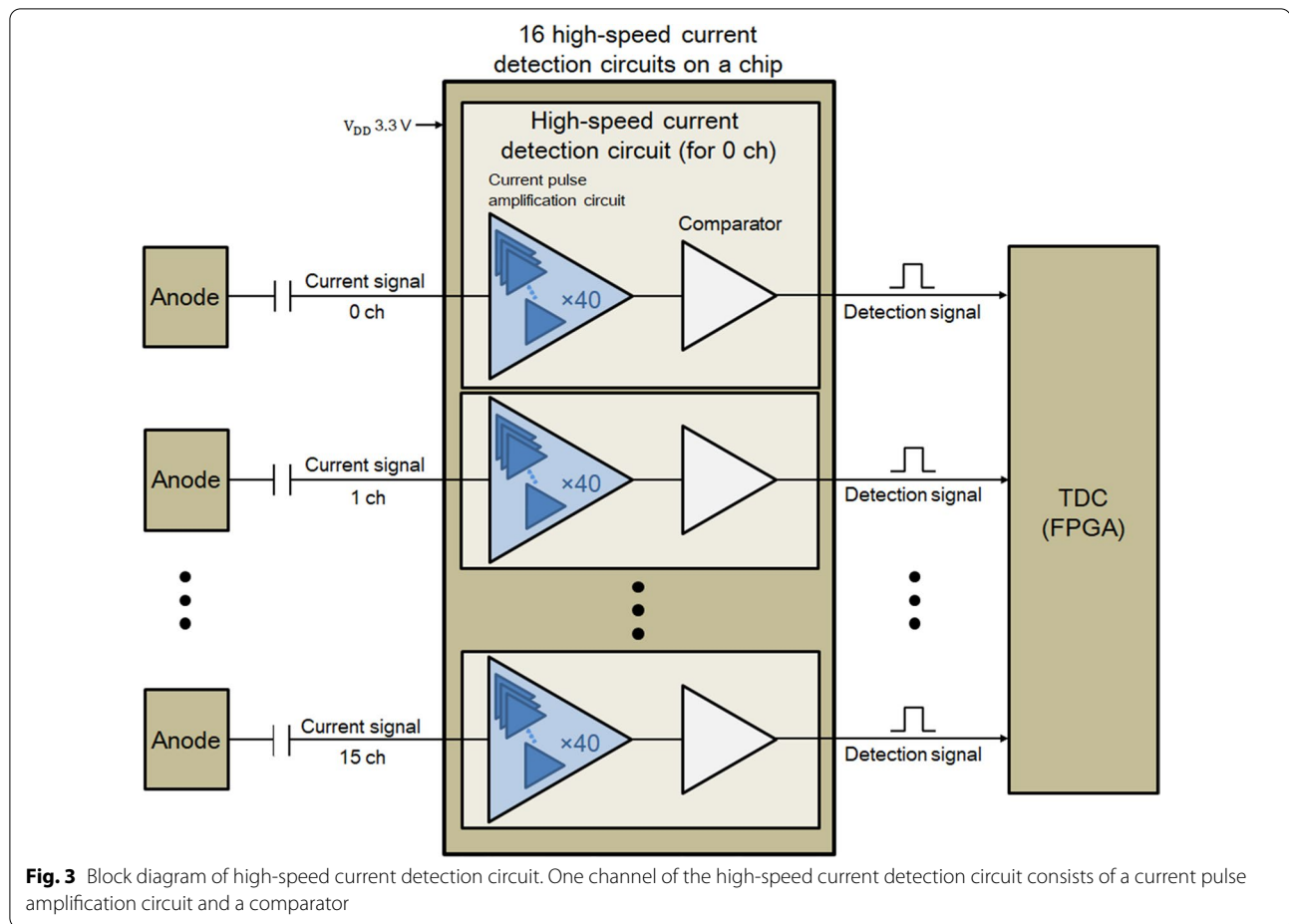
Figure 3 shows a block diagram of the high-speed current detection circuit. The circuit consists of a current pulse amplification circuit and a comparator. The first block amplifies an input pulse and converts it into a voltage signal. The comparator discriminates detection signals from noise and generates signals that are detectable by a TDC. The circuit is designed such that it can respond to an input current pulse with a duration of 1 ns.

The chip was developed using a complementary metal-oxide semiconductor (CMOS) 0.25 μm mixed-signal process by Taiwan Semiconductor Manufacturing Co., Ltd. The physical layout of one channel of the high-speed current detection circuit is shown in Fig. 4. The size of the current detection circuit is 530 μm × 210 μm. When we create a 4 × 8 circuit array with the high-speed

current detection circuits, the total size becomes 2120 μm × 1680 μm/32 channels.

Design of current pulse amplification circuit

A schematic diagram of the current pulse amplification circuit is shown in Fig. 5a. The circuit, which is powered by a single supply voltage of +3.3 V, consists of a bias circuit and main amplifier circuits. The bias circuit provides the gate voltage for CMOS transistors M1 and M2 in the main amplifier circuits. The main circuits receive an output pulse from an MCP at the input terminal V_{in} and amplify them with CMOS transistors M3 and M4. The output terminal V_{out_amp} is directly connected to the input of the comparator in the next stage. The CMOS parameters of the bias circuit are set such that the offset voltage of the input terminal V_{in} is 1.0 to 1.65 V, because the offset voltage at the input and output terminals should be half of the power supply voltage (+3.3 V) to achieve a wide dynamic range for the main amplifier circuits. The CMOS transconductance increases with the CMOS drain current. The drive current I_{ref} for the bias circuit is thus set to a maximum of 100 μA, which

Kikukawa *et al. Earth, Planets and Space*   *(2022) 74:188*

Page 5 of 11

Fig. 3 Block diagram of high-speed current detection circuit. One channel of the high-speed current detection circuit consists of a current pulse amplification circuit and a comparator

Fig. 4 Physical layout of the proposed high-speed current detection circuit

provides operation in the saturation region for all of the CMOS transistors.

We take 50 Ω as the input impedance of the current pulse amplification circuit to match the input impedance to the characteristic impedance of the coaxial cable that connects an MCP to a chip. The input impedance is mainly determined by the combined on-resistance ($r_{combined}$) of CMOS transistors M1 and M2. An arbitrary

$r_{combined}$ value can be obtained by selecting the channel width of M1 and M2. We conducted computer simulations to determine the relationship between $r_{combined}$ and the circuit response under the constraint that the total input impedance should be 50 Ω. In the simulations, we installed the same main amplifier circuits in parallel to realize an input impedance of 50 Ω for various values of $r_{combined}$. The simulated value of $r_{combined}$ required to achieve a rise time of close to 1 ns was 2 kΩ, which requires 40 main amplifier circuits to obtain an input impedance of 50 Ω.

Comparator design
The output signals of the current pulse amplification circuit are fed into a comparator in the next stage, as shown in Fig. 3. The comparator discriminates the input current from noise with the reference voltage V_{ref}. Figure 5b shows a schematic diagram of the comparator circuit. The comparator has a typical configuration that consists of a differential input, an amplification stage, and a buffer circuit. To determine the CMOS parameters, it was necessary to take into account an appropriate range of the
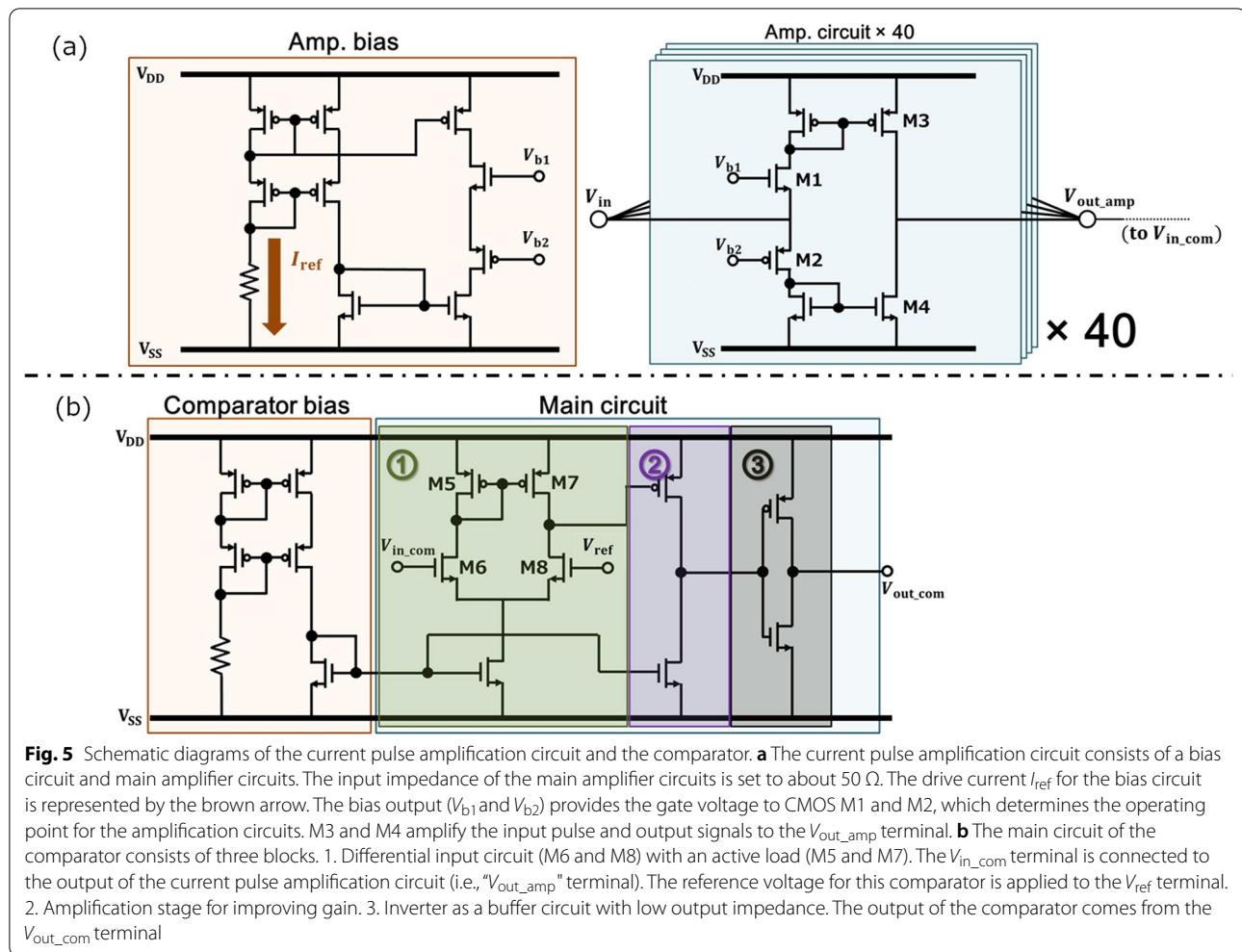
Kikukawa *et al. Earth, Planets and Space*   (2022) 74:188

Page 6 of 11

Fig. 5 Schematic diagrams of the current pulse amplification circuit and the comparator. **a** The current pulse amplification circuit consists of a bias circuit and main amplifier circuits. The input impedance of the main amplifier circuits is set to about 50 Ω. The drive current I_{ref} for the bias circuit is represented by the brown arrow. The bias output (V_{b1} and V_{b2}) provides the gate voltage to CMOS M1 and M2, which determines the operating point for the amplification circuits. M3 and M4 amplify the input pulse and output signals to the V_{out_amp} terminal. **b** The main circuit of the comparator consists of three blocks. 1. Differential input circuit (M6 and M8) with an active load (M5 and M7). The V_{in_com} terminal is connected to the output of the current pulse amplification circuit (i.e., "V_{out_amp}" terminal). The reference voltage for this comparator is applied to the V_{ref} terminal. 2. Amplification stage for improving gain. 3. Inverter as a buffer circuit with low output impedance. The output of the comparator comes from the V_{out_com} terminal

input common-mode voltage V_{CM} for the comparator. As described in Sect. 3.1, the offset voltage for the current pulse amplification circuit was designed to be 1.0 to 1.65 V. However, the offset voltage varied by several hundred millivolts due to variations in the characteristics of the CMOS transistors caused by manufacturing errors. Therefore, a wide range of V_{CM} was required for the comparator. We set the CMOS parameters to accomplish the V_{CM} range of 0.65 to 2.65 V.
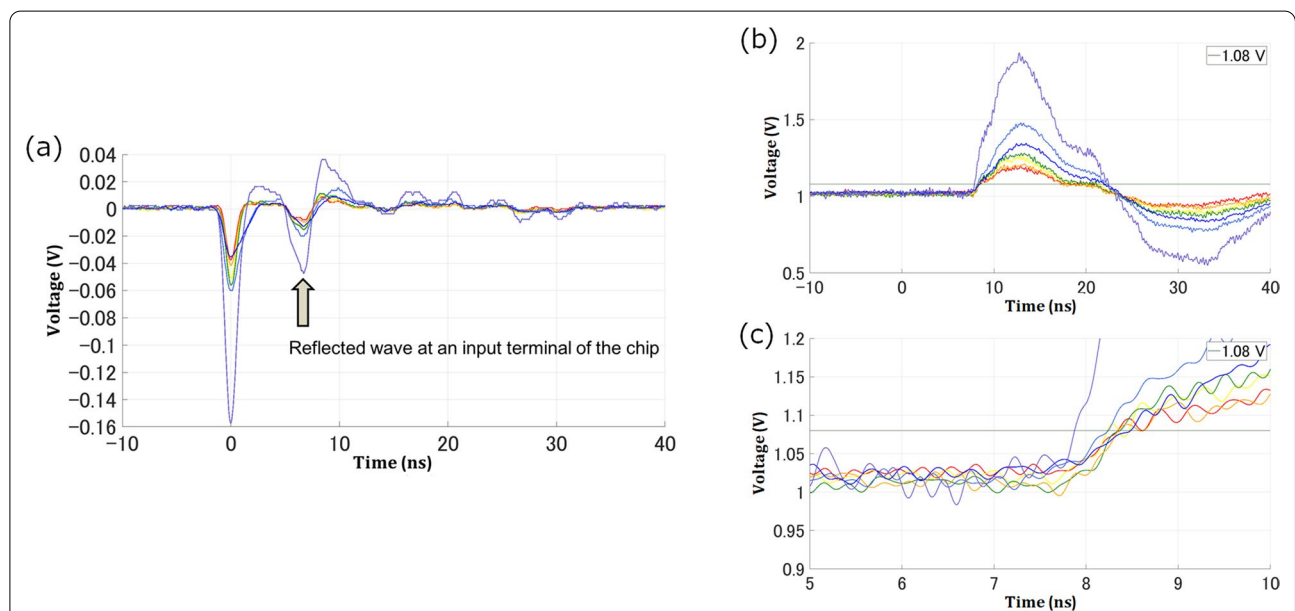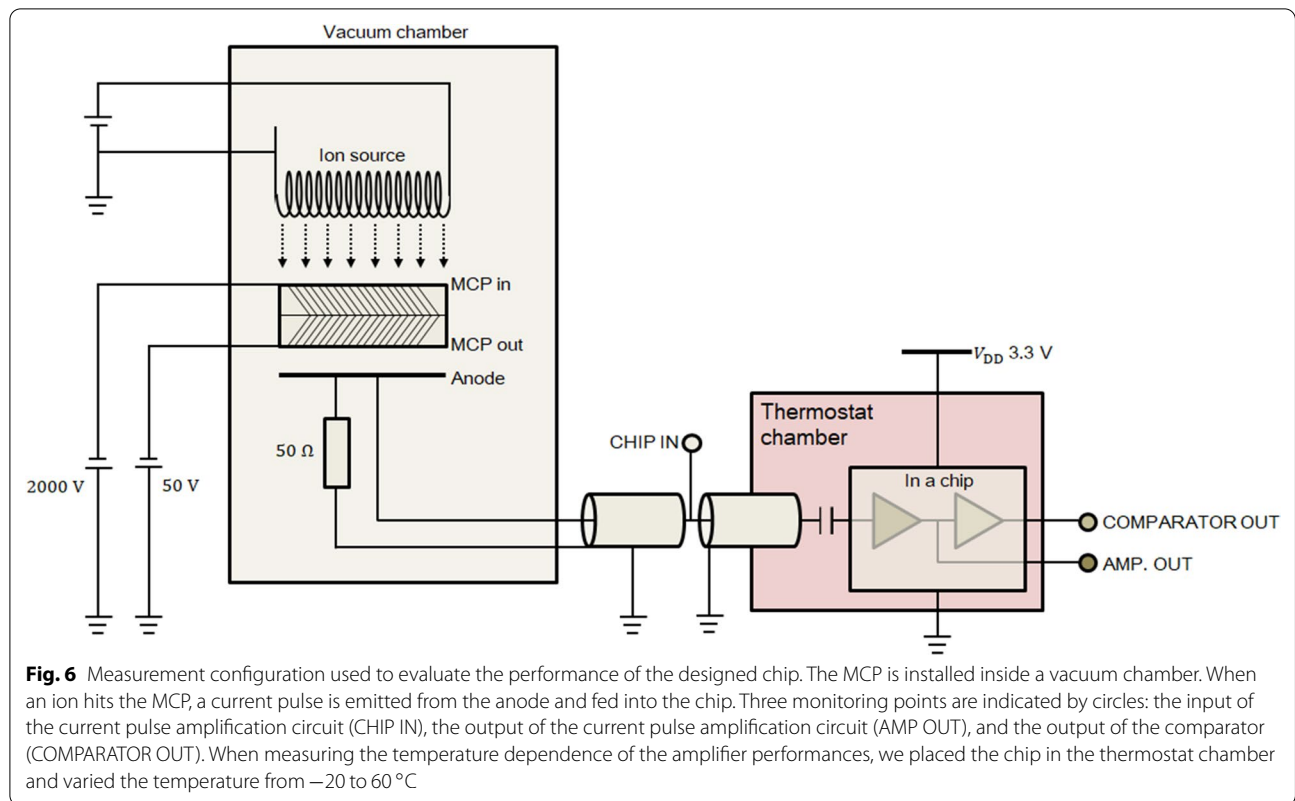
Performance of high-speed current detection circuit
This section describes the performance of the designed chip based on the results of laboratory experiments. Figure 6 shows a schematic view of the experimental configuration. The MCP was irradiated by ions emitted from an ion source in a vacuum chamber. The electron cloud released from the MCP was collected by the anode and became a current pulse. Termination with a 50 Ω resistance was applied to both ends of the transmission line between the anode and the input of the high-speed

current detection circuit (the circuit side was designed to have an internal input impedance of 50 Ω). Note that we used the thermostat chamber in Fig. 6 only when we evaluated the temperature dependence of the chip performances.

Current pulse amplification circuit
Figure 7a and b shows waveforms measured at monitoring points CHIP IN (input) and AMP. OUT (output), respectively (see Fig. 6). Figure 7c is a magnified view of Fig. 7b, focusing on the period of 5 to 10 ns. In Fig. 7, the input and output waveforms obtained with different input pulse heights are superimposed so that the peak timing for all input pulses is set to zero. The rise timings for the output waveforms are not significantly affected by the input pulse height, and thus the temporal variations of the output waveforms around 1.08 V (threshold voltage of the comparator input at the next stage) are suppressed to be less than 1 ns (see Fig. 7c). Secondary peaks appear in the input signals shown in Fig. 7a. They are the

Kikukawa *et al. Earth, Planets and Space* (2022) 74:188

Page 7 of 11

Fig. 6 Measurement configuration used to evaluate the performance of the designed chip. The MCP is installed inside a vacuum chamber. When an ion hits the MCP, a current pulse is emitted from the anode and fed into the chip. Three monitoring points are indicated by circles: the input of the current pulse amplification circuit (CHIP IN), the output of the current pulse amplification circuit (AMP OUT), and the output of the comparator (COMPARATOR OUT). When measuring the temperature dependence of the amplifier performances, we placed the chip in the thermostat chamber and varied the temperature from −20 to 60 °C

Fig. 7 Measured response of the current pulse amplification circuit. Waveforms were measured at the monitoring points (see Fig. 6). The time axis is defined so that the peak timing of the input waves is at 0 s. **a** Input pulse measured at CHIP IN, **b** output waveform measured at AMP. OUT, and **c** magnified view of panel **b** focusing on 5-10 ns. Seven waveforms in panel **a** show examples of input pulse heights from 35 mV to 200 mV, which include the highest one (i.e., the purple line) among all the measured waveforms. Each waveform in panels **b** and **c** corresponds to the waveform of the same color in panel **a**. In panel **a**, the wave reflected at the input terminal of the chip appears; it does not appear in panel **b** because it is absorbed at the MCP side. The timing variation of the cross-points between the output rising waveforms and 1.08 V is less than 1 ns (see panel **c**)

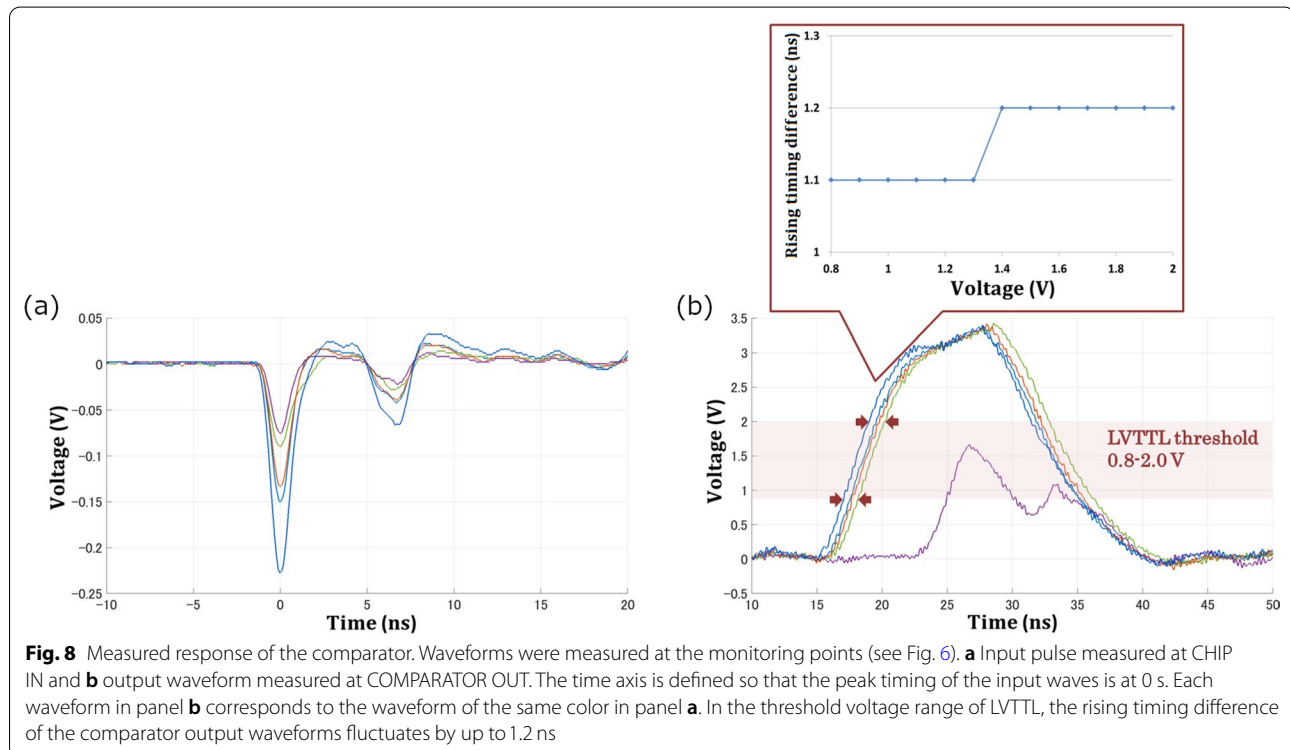Kikukawa *et al. Earth, Planets and Space*   (2022) 74:188

Page 8 of 11

input signals reflected at the terminal of the chip due to the impedance mismatch of the current pulse amplification circuit. Although the input impedance of the chip was designed to be 50 Ω, it was difficult to achieve precise impedance matching for the actual chip because of ASIC manufacturing errors. Since the reflected pulse was absorbed to ground at the anode through the termination resistance of 50 Ω, the reflection had no effect on the output of the current pulse amplification circuit.

Comparator

The comparator receives the output of the current pulse amplification circuit. The comparator discriminates the output signal of the current pulse amplification circuit from noise with the reference voltage $V_{\rm ref}$. The output of the current pulse amplification circuit shown in Fig. 7b had an offset of 1.0 V; the minimum pulse height was approximately 1.2 V. Consequently, we set $V_{\rm ref}$ to 1.22 V to detect almost all input signals to the chip. Note that the reference voltage for the comparator was 1.22 V (not 1.08 V) because there was an offset at the comparator differential input terminal. Figure 8b shows the response of the comparator observed at monitoring point COMPARATOR OUT (see Fig. 6) when the current pulses shown in Fig. 8a were input to the ASIC and $V_{\rm ref}$ was fixed at 1.22 V. The blue line (the height of the input pulse to the ASIC is 230 mV) represents the case where the signal

from the MCP was the strongest and the yellow line (the height of the input pulse is 85 mV) represents the case where the signal from the MCP was the weakest among the signals that could be detected by the comparator. The area highlighted in red in Fig. 8b shows the typical LVTTL threshold voltage range. The fluctuation of the rising output timing, except for the case where the height of the input pulse to the comparator is close to $V_{\rm ref}$ (purple line), is less than 1.2 ns in the range of 0.8 to 2.0 V, which is slightly below the performance requirement. However, considering that the time resolution required for the LEPi is above 1.6 ns, as described in Sect. 2, this ASIC-based amplifier can still be used for TOF-based mass analysis. Here, it is necessary to distinguish the case where the pulse height of the comparator output is less than 3.3 V such as the purple line in Fig. 8b from the other patterns, since the time variation of the comparator output is much more than 1 ns when the input pulse height is close to $V_{\rm ref}$. One possible solution is to apply two comparators with different $V_{\rm ref}$ values at the output of the current pulse amplification circuit. We could distinguish input signals with a pulse height of close to $V_{\rm ref}$ if we applied a higher $V_{\rm ref+}$ for the additional comparator.

We conducted an experiment to measure the temperature dependence of the developed amplifier in terms of the detectable input level, sensitivity, and time walk. The experimental configuration is shown in Fig. 6. We varied
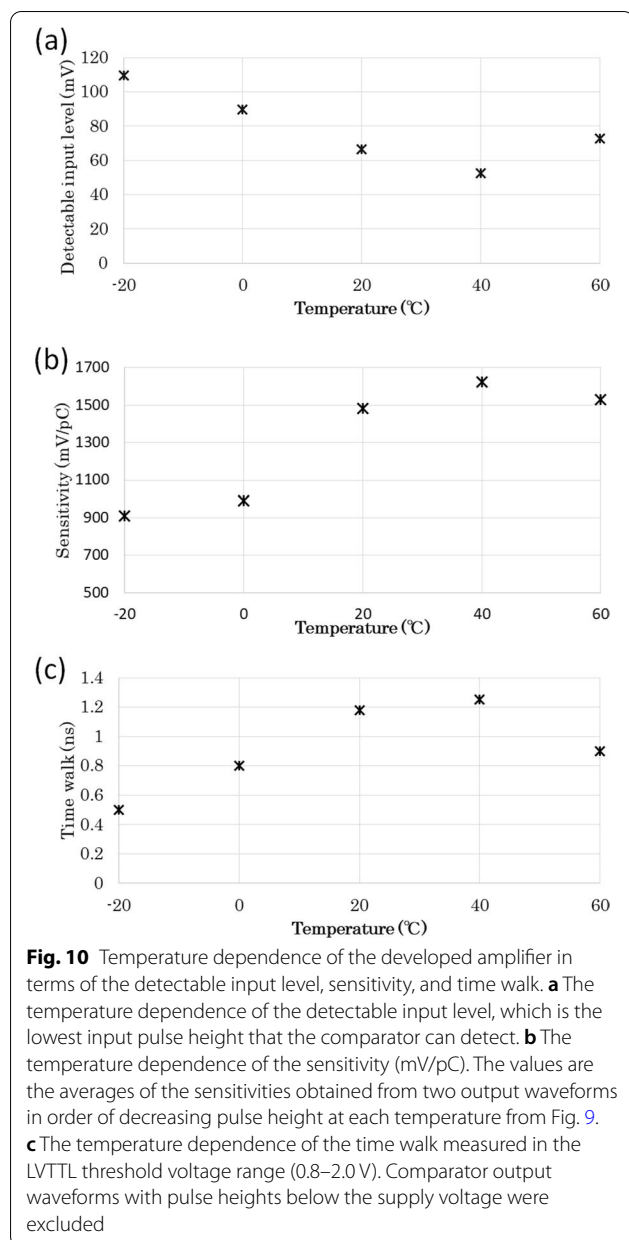

Fig. 8 Measured response of the comparator. Waveforms were measured at the monitoring points (see Fig. 6). **a** Input pulse measured at CHIP IN and **b** output waveform measured at COMPARATOR OUT. The time axis is defined so that the peak timing of the input waves is at 0 s. Each waveform in panel **b** corresponds to the waveform of the same color in panel **a**. In the threshold voltage range of LVTTL, the rising timing difference of the comparator output waveforms fluctuates by up to 1.2 ns

Kikukawa *et al. Earth, Planets and Space*　　*(2022) 74:188*

Page 9 of 11

Fig. 9 Input/output waveforms measured at −20 to 60 °C. 5–6 waveforms measured at each temperature are superimposed so that the peak timing of the input waveforms is at 0 s. These waveforms show examples of input pulse heights of about 200, 180, 150, 120, and 90 mV and the weakest signal that can be detected by the comparator, respectively. For the experiments conducted at −20 °C, the comparator could not detect input signals with a pulse height of below 90 mV; these signals are thus not shown in panel **a**

the temperature inside the chamber from −20 to 60 °C in 20 °C steps and measured the input/output waveforms for the chip. Note that the comparator reference voltage was consistent throughout this experiment.

Figure 9 shows the input and output waveforms measured at different temperatures. We selected 5–6 waveforms at each temperature, including that with the strongest input signal (pulse height: about 200 mV) and that with the weakest one, where the output pulse height for the comparator was almost equal to the supply voltage (+3.3 V). These waveforms are superimposed so that the peak timings of the input waveforms are at 0 s. If we define the detectable input level for the amplifier as the lowest input pulse height when the comparator output reaches the supply voltage, the temperature dependence of the input level changes as shown in Fig. 10a. To obtain the temperature dependence of the sensitivity of this

amplifier, we selected two output waveforms in order of decreasing pulse height at each temperature from Fig. 9. We have calculated input charge assuming the input impedance of the high-speed current detection circuit to be 50 Ω. Using the measurement results of input voltage to the chip (shown in Fig. 9), we can obtain the amount of charge flowing from the MCP into the chip at each measurement time. We have derived the total amount of input charge by integrating the amount of charge over the duration of the input pulse. The results regarding the calculated sensitivity of the amplifier are shown in Fig. 10b. The sensitivity improves with increasing temperature, which is consistent with the results in Fig. 10a, where the detectable input level decreases with increasing temperature. The temperature dependence of the time walk (i.e., rising timing difference of the comparator output) is shown in Fig. 10c. Note that comparator output

Kikukawa *et al. Earth, Planets and Space*　　*(2022) 74:188*

Page 10 of 11

Fig. 10 Temperature dependence of the developed amplifier in terms of the detectable input level, sensitivity, and time walk. **a** The temperature dependence of the detectable input level, which is the lowest input pulse height that the comparator can detect. **b** The temperature dependence of the sensitivity (mV/pC). The values are the averages of the sensitivities obtained from two output waveforms in order of decreasing pulse height at each temperature from Fig. 9. **c** The temperature dependence of the time walk measured in the LVTTL threshold voltage range (0.8–2.0 V). Comparator output waveforms with pulse heights below the supply voltage were excluded

Thus, the maximum count rate detectable by the high-speed current detection circuit is more than 2×10^7/s, which is higher than the target count rate (1×10^7/s).

Conclusion

We developed an ultra-small high-speed current detection circuit based on ASIC technology for satellite-borne instruments for space plasma measurements. The current detection circuit amplifies the feeble electron cloud coming from an MCP so that a TDC can perform TOF calculations. The measured sensitivity 1.5 V/pC is comparable with the sensitivity 1 V/pC of commercially available pre-amplifiers of a significantly larger size. The estimated area of the developed current detection circuit with 32 channels is 2120 μm $\times$ 1680 μm, which allows the circuit to be integrated into a 15 mm square package. Laboratory experiments show that the developed circuit can respond to an MCP signal with a timing variation of better than 1.2 ns, making it applicable to TOF calculations. In addition, the signal processing rate can be more than 2×10^7 signals per second since the time interval between the arrival of the input pulse and the end of the output pulse is less than 45 ns. The developed circuit can be used for conventional TOF-based ion energy-mass spectrometers for space plasmas. The reduction of instrument size will contribute to the future realization of simultaneous multi-point measurements of space plasmas.

waveforms with pulse heights below the supply voltage were excluded. The time walk at each temperature shown in Fig. 10c was estimated from the maximum value of the time walk in the LVTTL threshold voltage range (0.8 to 2.0 V). Figure 10c shows that the amplifier achieves the required timing resolution (≤ 1.6 ns) to perform TOF measurements in the temperature range of -20 to 60 °C.

The time interval between the arrival of the input pulse and the end of the output pulse is less than 45 ns, which means that the comparator returns to its initial state within 45 ns from the arrival of the input signals to the chip.

Kikukawa *et al. Earth, Planets and Space*　　　*(2022) 74:188*

Page 11 of 11

Declarations

Ethics approval and consent to participate
Not applicable.

Consent for publication
Not applicable.

Competing interests
The authors declare that they have no competing interests.

Author details
[1]Research Institute for Sustainable Humanosphere, Kyoto University, Gokasho, Uji 611-0011, Japan. [2]Institute of Space and Astronautical Science, Japan Aerospace Exploration Agency, 3-1-1 Yoshinodai, Chuo, Sagamihara 252-5210, Japan. [3]National Institute of Technology, Nara College, 22 Yatacho, Yamatokori-yama, Nara 639-1080, Japan.

References

Angelopoulos V et al (2008) First results from the THEMIS mission. Space Sci Rev 141(1):453–476. https://doi.org/10.1007/s11214-008-9378-4

Asamura K et al (2003) Auroral particle instrument onboard the INDEX satellite. Adv Space Res 32(3):375–378. https://doi.org/10.1016/S0273-1177(03)90275-4

Asamura K et al (2018) Low-energy particle experiments–ion mass analyzer (LEPi) onboard the ERG (Arase) satellite. Earth Planets Space 70(1):1–15. https://doi.org/10.1186/s40623-018-0846-0

Asamura K et al (2021) Cross-energy couplings from magnetosonic waves to electromagnetic ion cyclotron waves through cold ion heating inside the plasmasphere. Phys Rev Lett 127(24):245101. https://doi.org/10.1103/PhysRevLett.127.245101

Burch JL et al (2016) Magnetospheric multiscale overview and science objectives. Space Sci Rev 199(1):5–21. https://doi.org/10.1007/s11214-015-0164-9

Carlson, C.W. and McFadden, J.P. (1998). Design and application of imaging plasma instruments. In: Measurement techniques in space plasmas: particles (eds R.F. Pfaff, J. Borovsky and D.T. Young) DOI:https://doi.org/10.1029/GM102p0125

Carlson CW et al (2001) The electron and ion plasma experiment for FAST. The FAST mission. Springer, Dordrecht, pp 33–66

Escoubet CP, Fehringer M, Goldstein M (2001) Introduction the cluster mission. Ann Geophys 19(1012):1197–1200

Gloeckler G et al (1985) First composition measurement of the bulk of the storm-time ring current (1 to 300 keV/e) with AMPTE-CCE. Geophys Res Lett 12(5):325–328. https://doi.org/10.1029/GL012i005p00325

Katoh Y et al (2013) Significance of wave-particle interaction analyzer for direct measurements of nonlinear wave-particle interactions. Ann Geophys. https://doi.org/10.5194/angeo-31-503-2013

Keika K et al (2022) Preferential energization of lower-charge-state heavier ions in the near-earth magnetotail. J Geophys Res Space Phys 127(1):e2021JA029786. https://doi.org/10.1029/2021JA029786

Kitamura N et al (2018) Direct measurements of two-way wave-particle energy transfer in a collisionless space plasma. Science 361(6406):1000–1003. https://doi.org/10.1126/science.aap8730

Maggiolo R, Kistler LM (2014) Spatial variation in the plasma sheet composition: dependence on geomagnetic and solar activity. J Geophys Res Space Phys 119(4):2836–2857. https://doi.org/10.1002/2013JA019517

Miyoshi Y et al (2018) Geospace exploration project ERG. Earth Planets Space 70(1):1–13. https://doi.org/10.1186/s40623-018-0862-0

Ozaki M et al (2016) Development of an ASIC preamplifier for electromagnetic sensor probes for monitoring space electromagnetic environments. Earth Planets Space 68(1):1–13. https://doi.org/10.1186/s40623-016-0470-9

Pollock C et al (2016) Fast plasma investigation for magnetospheric multiscale. Space Sci Rev 199(1):331–406. https://doi.org/10.1007/s11214-016-0245-4

Rauch JL, Roux A (1982) Ray tracing of ULF waves in a multicomponent magnetospheric plasma: consequences for the generation mechanism of ion cyclotron waves. J Geophys Res Space Phys 87(A10):8191–8198. https://doi.org/10.1029/JA087iA10p08191

Saito Y et al (2017) High-speed MCP anodes for high time resolution low-energy charged particle spectrometers. J Geophys Res Space Phys 122(2):1816–1830. https://doi.org/10.1002/2016JA023157

Shelley EG, Johnson RG, Sharp RD (1972) Satellite observations of energetic heavy ions during a geomagnetic storm. J Geophys Res 77(31):6104–6110. https://doi.org/10.1029/JA077i031p06104

Shoji M et al (2021) Discovery of proton hill in the phase space during interactions between ions and electromagnetic ion cyclotron waves. Sci Rep 11(1):1–8. https://doi.org/10.1038/s41598-021-92541-0

Summers D, Thorne RM (2003) Relativistic electron pitch-angle scattering by electromagnetic ion cyclotron waves during geomagnetic storms. J Geophys Res Space Phys. https://doi.org/10.1029/2002JA009489

Tooley CR et al (2016) The magnetospheric multiscale constellation. Space Sci Rev 199(1):23–76. https://doi.org/10.1007/s11214-015-0220-5

Williams DJ (1981) Ring current composition and sources: an update. Planet Space Sci 29(11):1195–1203. https://doi.org/10.1016/0032-0633(81)90124-0

Wüest M (1998) Time-of-flight ion composition measurement technique for space plasmas. In: Pfaff RF, Borovsky J, Young DT, Eds. Measurement techniques in space plasmas: particles. https://doi.org/10.1029/GM102p0141

Wurz P (2000) Detection of energetic neutral particles. In: Scherer K, Fichtner H, Marsch E (eds) The outer heliosphere: beyond the planets. Copernicus Gesellschaft e.V, Katlenburg-Lindau, pp 251–288

Young DT, Balsiger H, Geiss J (1982) Correlations of magnetospheric ion composition with geomagnetic and solar activity. J Geophys Res Space Phys 87(A11):9077–9096. https://doi.org/10.1029/JA087iA11p09077

Zushi T et al (2019) Development of a miniaturized spectrum-type plasma wave receiver comprising an application-specific integrated circuit analog front end and a field-programmable gate array. Meas Sci Technol 30(5):055901. https://doi.org/10.1088/1361-6501/ab0821

Publisher's Note

Springer Nature remains neutral with regard to jurisdictional claims in published maps and institutional affiliations.